Angular dependent FORC and FMR of exchange-biased NiFe multilayer films

R A Gallardo[1], S Khanal[2], J M Vargas[3], L Spinu[2], C A Ross[4] and C Garcia[1]

[1] Departamento de Física, Universidad Técnica Federico Santa María, Avenida España 1680, 2390123 Valparaíso, Chile
[2] Advanced Materials Research Institute (AMRI) and Department of Physics, University of New Orleans, New Orleans, LA 70148, USA
[3] Centro Atómico Bariloche (CNEA), Instituto Balseiro (U. N. Cuyo) and Conicet, 8400 San Carlos de Bariloche, Río Negro, Argentina
[4] Department of Materials Science and Engineering, Massachusetts Institute of Technology, Cambridge, MA, USA

E-mail: carlos.garcia@usm.cl

CrossMark

Abstract

Dynamic ferromagnetic resonance (FMR, X-band 9.8 GHz) and static first-order reversal curve (FORC) techniques are combined to study the intrinsic exchange-bias distribution via measurements of in-plane angular variation in (FeNi/IrMn)n multilayers. The angular dependence of the exchange bias field was qualitatively and quantitatively investigated using both methods, which are sensitive to different couplings between the ferromagnetic layers. We have used the analysis of the angular dependence of first-order reversal curve (AFORC) data, extracted from FORC curves measured from 0° up to 360° in 10° steps. In addition, its counterpart angular dependence of FMR (AFMR) measurements were carried out and correlated with the AFORC results.

The AFORC proved to be useful for simultaneously studying the magnetization reversal processes and magnetic interactions between the layers of the (FeNi/IrMn)n. These interactions are related to the structure and interfaces in the (FeNi/IrMn), and the results obtained by AFMR and AFORC are contrasted with a modified theoretical model for domain-wall formation.

Keywords: exchange-bias, ferromagnetic resonance, first-order reversal curves

(Some figures may appear in colour only in the online journal)

Introduction

Interfacial coupling between antiferromagnetic (AFM) and ferromagnetic (FM) materials is well known to cause a magnetic hysteresis loop shift known as exchange-bias (EB) [1–5]. This phenomenon has enabled a great variety of spintronic applications such as giant magnetoresistance- or tunneling magneto-resistance-based sensors and magnetic random access memory [6], and microwave devices operating in the gigahertz range [7–9]. Because of its technological impact, exchange-biased structures have been widely addressed from the theoretical and experimental point of view, but there are still ongoing controversies about the mechanism of EB owing to incomplete

knowledge of the structure and coupling at the AFM/FM interface [4, 10]. An early single-domain model with unidirectional anisotropy was proposed by Meiklejohn and Bean to explain the hysteresis shift [1]. Later, Mauri *et al* introduced a planar domain wall in the AFM layer which led to a reduction of the bias field by reducing the energy required to reverse the magnetization [11]. Malozemoff, considering the interface roughness, used a random field model to explain the reduction of the exchange-bias [12]. Interfacial disorder has been addressed by using Monte Carlo calculations [13–16]. Other authors have quantitatively studied the role of two-magnon scattering, activated by geometric defects, in exchange-biased bilayers [17, 18], and Stiles and McMichael introduced the

J. Phys. D: Appl. Phys. **50** (2017) 075002

R A Gallardo *et al*

concept of rotatable anisotropic field H_{RA} to explain the enhancement of the coercivity and EB of the AFM/FM system [19]. Since the rotatable field originates from inhomogeneities in the AFM layer, where magnetic moments are able to follow the external field during the rotation, a dynamic measurement procedure is required to determine the value of H_{RA}, such as measurement of ferromagnetic resonance (FMR). Some differences between static and dynamic magnetic anisotropies have been previously attributed to H_{RA} [20], and therefore, both dynamic and static magnetic measurements are required to fully investigate the features of exchange-biased systems.

The static magnetic properties can be revealed through magnetometry measurements following major hysteresis loops (MHL) and first-order reversal curves (FORC) protocols. Although MHL parameters such as coercivity, saturation magnetization and remanence are useful parameters, they represent global sample averages and are not appropriate to describe heterogeneous magnetic samples such as multilayer films or granular samples. In such materials it is of great interest to identify the different magnetic contributions coming from each of the constituents and interactions between them. The collective behaviour of a multilayer structure will in general differ from that of the individual layers due to interactions.

The FORC method provides more information about magnetization reversal than MHL measurements do, including distributions of coercive and interaction fields. This technique can be particularly efficient and powerful in the case of highly interacting systems [21]. As we will show, the supplementary information provided by FORC diagrams and its angular variation are essential in correlating the observed EB field distribution with sample characteristics such as inherent inhomogeneities existing at the AFM/FM interfaces.

Mayergoyz first proposed FORC as an experimental method for the determination of the Preisach distribution of a system described by the classical Presach model [22–24], in which the hysterons do not necessarily relate to actual physical entities.

Pike *et al* extended this interpretation beyond the classical Preisach model, developing the FORC diagram method [25] and focusing on the various signatures seen in experimental FORC diagrams of different types of samples. It has also been shown that some parameters of the FORC distributions may be used to distinguish between the average magnetic properties of the entities constituting the system and the magnetic interactions between them.

Over recent years, experimental use of the FORC method has expanded considerably. The principal difficulty during the experimental use of the FORC method resides in the correct identification of the physical meaning of the mathematical hysterons [26]. Thus, a proper interpretation and system modeling is a critical issue. For example, Rotaru *et al* [27] studied the effect of dipolar interaction by the FORC method in several series of Ni nanowires arrays with controlled spatial distribution. For some nanowire geometries, FORC analysis was indicative of a reversal-field memory effect.

Liu *et al* [28], used a FORC method to capture magnetic fingerprints of Fe nanodots as they underwent a single domain to vortex state transition. As the nanodot size increased, the FORC diagrams revealed striking differences, despite only

subtle changes in their major hysteresis loops. Focusing on the nucleation and saturation processes, Liu *et al* [29] also investigated the magnetization reversal process in Co/Pt multilayers with perpendicular magnetic anisotropy by the FORC technique. They observed that the onset of magnetization reversal was dominated by irreversible processes, corresponding to the avalanche-like propagation of one-dimensional stripe domains originated from earlier nucleated zero-dimensional bubble domains.

Previously our group [30] performed a systematic FORC study of the IrMn/FeNi multilayer system. The aim was to correlate the static and dynamic properties by using different magnetic measurement techniques up to 25 GHz. These experiments were conducted along only one direction: the easy axis parallel to the exchange-bias field direction. Also, the previous study focused on the main ferromagnetic resonance modes and did not discuss the additional FMR modes or their linewidth.

The angular FORC (AFORC) technique was recently introduced by Proenca *et al* [31], to offer additional information on the angular dependence of the magnetostatic and interphase interactions of Co nanowires and nanotubes. Using AFORC, one is able to simultaneously study magnetization reversal processes and magnetic interactions between the nanomagnets and to obtain the interaction field distribution (IFD) and the coercive field distribution (CFD) through cross sections of the 2D AFORC diagrams. For example, Kashi *et al* studied the angular variation and evolution of the IFD and CFD profiles of Co nanowire arrays in which two magnetic populations related to the Co crystalline directions were superimposed. From the AFORC data they observed that the demagnetizing interaction between the two populations led to additional features in the FORC diagrams. Changes in the magnetic behavior from interacting to non-interacting were clearly observed in the evolution of the IFD and CFD profiles [32, 33].

Here we report a comprehensive study of the angular variation and the correlation between static and dynamic measurements in (FeNi/IrMn)n multilayers. Both FORC and FMR techniques are used to study the in-plane angular variation of magnetic properties and the results are related to a modified theoretical model for domain-wall formation [11, 34].

Experimental procedure

Several configurations of multilayer systems (FeNi(t_{FeNi} nm)/ IrMn (20 nm)) $n(t)$, with $t_{FeNi} = 20$ nm, 60 nm, 80 nm and $n = 10, 5, 4$, respectively, were fabricated, with the same total thickness [30]. The films were deposited on thermally oxidized Si(1 0 0) substrates using dc-triode sputtering at ambient temperature with a base pressure of 3×10^{-9} Torr. Layers were deposited using an Ar pressure of 1 mTorr. The magnetic thin film was deposited from a stoichiometric target of 80–20 at % FeNi. The films were growth on a Ti(10 nm) seed layer and capped with 10 nm of Ti. Longitudinal magnetic anisotropy was induced by applying a magnetic field of 250 Oe along the long axis of the strips during deposition.

J. Phys. D: Appl. Phys. **50** (2017) 075002

R A Gallardo *et al*

Table 1. Structural information of the samples S1, S2 and S3, where *t* is the layer thickness and *n* is the number of repetitions.

	Multilayer structure		
	FeNi *t* (nm)	IrMn *t* (nm)	Repetition # *n*
S1	20	20	10
S2	60	20	5
S3	80	20	4

Table 1 summarizes the structural information of these multilayer films. All the samples showed an in-plane easy axis, with unidirectional exchange-bias at room temperature. The same samples also exhibited a linear response of the magnetoimpedance (MI) at zero field which is advantageous for sensor applications [35, 36].

The MHL and angular FORC measurements were conducted on a Princeton AGM–VSM (Model 3900) magnetometer using the VSM mode at room temperature. The magnetic field was applied in plane along the easy axis of the samples, and every 10°. The magnetometer is optimized for this type of FORC measurements, where it can record a set of 100 FORCs in less than 2 h, with a typical sensitivity of 0.5 μemu and 1 s average time per point. A discrete sweep mode (point-by-point) and pause time of 1 s at the H_{res} resonance field were used. The FORC data was later analyzed by using FORCinel.

A Bruker EMX FMR spectrometer operating at 9.87 GHz (X-band) was used to perform the X-band FMR measurements at room temperature, microwave power of 3.17 mW, with the magnetic field driven from $H = 0$ Oe to 2 kOe in 42 s sweep time (163 Oe s^{-1}). Angle-dependent FMR experiments were carried out for each sample with a step size of $\Delta\varphi = 3°$. By fitting a typical Lorentzian single-line absorption to the derivative of the FMR spectrum, two characteristic parameters could be determined, i.e. the resonant field H_{res}, and the linewidth.

Theoretical description

FORC distribution and diagrams

As detailed in [30], the FORC measurement starts from a positive saturation of the samples followed by sweeping down the magnetic field to a reversal value H_R. The magnetic field is then increased up to saturation and the magnetization is measured as a function of the applied field H. The magnetization obtained in the applied field H after each field reversal at H_R, $M(H, H_R)$, determines a family of FORCs. The normalized FORC distribution is obtained as:

$$\rho(H, H_R) = -\frac{1}{2M_s}\frac{\partial^2 M(H, H_R)}{\partial H_R \partial H}, \qquad (1)$$

where M_s is the saturation magnetization of the sample.

The FORC distribution and its contour plots i.e. the FORC diagrams, were obtained using FORCinel. FORCinel has a subroutine that eliminates the swept field valley artifact at the beginning of the loops, which was used here to obtain

the FORC diagrams. FORC distributions and diagrams were represented in terms of the local coercivity (h_c) and bias (h_u) defined as $h_c = (H - H_R)/2$ and $h_u = (H + H_R)/2$. In-plane AFORCs were then obtained by changing the angle from 0° up to 360° in 10° steps, and measuring a complete set of FORCs for each angle.

FMR theory

A modified domain-wall formation (DWF) model [11, 34] is used in the theoretical description, where is assumed that a magnetic domain wall is created at the AFM interface while the FM film is rotated in a field. Non-collinearity between the magnetization of the AFM sublattice in contact with the FM ($\mathbf{M}_{AF}$) and the FM equilibrium magnetization of the free layer is allowed. The free energy per unit volume is given by [17, 34]

$$\epsilon = -\mathbf{H} \cdot \mathbf{M} + \left(2\pi M_s^2 - \frac{K_s}{t_{FM}}\right)(\hat{\mathbf{M}} \cdot \hat{y})^2 - K_U(\hat{\mathbf{M}} \cdot \hat{u}_K)^2$$
$$- \frac{J_E}{t_{FM}}\hat{\mathbf{M}} \cdot \hat{\mathbf{M}}_{AF} - \frac{\sigma_W}{t_{FM}}\hat{\mathbf{M}}_{AF} \cdot \hat{u}_{AK} - \mathbf{H}_{RA} \cdot \mathbf{M}, \qquad (2)$$

where $\mathbf{H}$ is the external field, K_U (K_s) is the uniaxial (surface) anisotropy constant, t_{FM} is the FM thickness, J_E is the interfacial exchange energy per unit area and σ_W is the energy per unit surface of a 90° domain wall in the AFM. In addition, H_{RA} is the rotatable anisotropy field [19], which represents an additional uniaxial anisotropy with its axis oriented along the external field. The unit vectors $\hat{y}$, $\hat{u}_K$ and $\hat{u}_{AK}$ represent the normal to the film plane, the uniaxial anisotropy direction, and the AFM pinning direction, respectively.

Thus, following Smit and Beljers [37] the ferromagnetic resonance (FMR) frequency can be written as

$$\Omega = \gamma\sqrt{H_{XX}H_{YY}}, \qquad (3)$$

where γ is the gyromagnetic ratio and the stiffness fields H_{XX} and H_{YY} are given by [17]

$$H_{XX} = H + H_K \cos^2(\varphi - \varphi_K) + 4\pi M_{eff} + H_{RA} + H_1$$

and

$$H_{YY} = H + H_K \cos 2(\varphi - \varphi_K) + H_{RA} + H_2.$$

Here, $H_K = 2K_u/M_s$ is the uniaxial anisotropy field and $4\pi M_{eff} = 4\pi M_s - H_s$, where $H_s = 2K_s/(M_s t_{FM})$ is the surface anisotropy field. As shown in figure 1, the in-plane angles φ and φ_K indicate the orientation of the FM magnetization $\mathbf{M}$ and the uniaxial in-plane easy axis $\hat{u}_K$ with respect to the *z*-axis, respectively. It is assumed that the resonant field is strong enough so that $\varphi \approx \varphi_H$, where φ_H is the angle between the external field and the *z*-axis.

The fields H_1 and H_2 are given by [17, 38]

$$H_1 = H_{eb}\frac{H_W \cos(\varphi - \varphi_A) - H_{eb}\sin^2(\varphi - \varphi_A)}{H_W \cos(\varphi_A - \varphi_{AK}) + H_{eb}\cos(\varphi - \varphi_A)} \qquad (4)$$
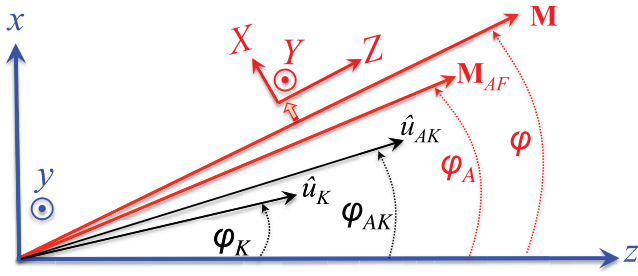
and

Figure 1. In-plane geometry considered in the theory. Vectors $\hat{u}_K$, $\hat{u}_{AK}$, $\mathbf{M}_{AF}$ and $\mathbf{M}$ have in-plane arbitrary orientations and they make an angle φ_K, φ_{AK}, φ_A and φ with the z axis, respectively. φ_A and φ_{AK} are the angles that $\mathbf{M}_{AF}$ and the antiferromagnetic pinning direction $\hat{u}_{AK}$, respectively, form with the z-axis. The coordinate system (X, Y, Z) is defined in such a way that the Z axis points along the equilibrium magnetization and the X axis always lies in the film plane.

$$H_2 = H_{eb}\frac{H_W \cos(\varphi_A - \varphi_{AK})\cos(\varphi - \varphi_A)}{H_W \cos(\varphi_A - \varphi_{AK}) + H_{eb}\cos(\varphi - \varphi_A)}. \quad (5)$$

Here, $H_{eb} = J_E/(M_s t_{FM})$ is the exchange-bias field and $H_W = \sigma_W/(M_s t_{FM})$ is the domain wall effective field. Note that the field H_W, which appears due the existence of an AFM domain wall in exchange-coupled systems, is included to take into account the 10^{-2} reduction of the exchange field from the ideal interface model case [11, 12, 19, 38]. $\mathbf{M}_{AF}$ corresponds to the magnetic moments in the AFM sublattice adjacent to the FM layer. By using equation (3), the resonance field is obtained:

$$H_{res} = \frac{1}{2}\Big\{H_K\big[1 - 3\cos^2(\varphi - \varphi_K)\big] - F_{eff}^+ - 2H_{RA}$$
$$+ \sqrt{\big[H_K\sin^2(\varphi - \varphi_K) + F_{eff}^-\big]^2 + 4(\Omega/\gamma)^2}\Big\}, \quad (6)$$

where $F_{eff}^{\pm} = 4\pi M_{eff} + H_1 \pm H_2$. From equation (6), we note that H_{res} depends on the exchange-bias field H_{eb}. Therefore, in a multilayer system where each layer could have its own exchange coupling field H_{eb}, more than one resonant mode is expected, which will be discussed in the next section. The angular dependence of the exchange-bias field can be described as [38]

$$H_{eb}(\varphi) = \frac{1}{2}\left[H_{res}(\varphi) - H_{res}(\pi + \varphi)\right]. \quad (7)$$

For $\varphi = 0$, $H_{eb}(0)$ depends on both H_{eb} and H_W, nevertheless under the condition $H_W \gg H_{eb}$, $H_{eb}(0) \approx H_{eb}$.

Results and discussion

AFORC diagrams and profiles

Based on the major hysteresis loops of samples S1, S2, and S3, to obtain good resolution FORC data, the values of the average measuring-time, number of FORC loops, and the field-step of these measurements were set at 0.2 s per point, 250 curves, and 0.8 Oe, respectively. Initially, the smoothing factor was chosen using FORCinel's optimal smoothing factor

routine, based on the residuals of the FORC diagram [39]. However, it was found that the optimal smoothing factor was unreasonable high (at 40° optimal smoothing factor was found to be SF = 7 (sample S1), SF = 5 (sample S2), and SF = 4 (sample S3)) and for consistency all the FORC distributions were displayed with a fixed smoothing factor of SF = 3.

Figure 2 shows the results for sample S1, of the angular first order reversal curves (left) and their respective 2D FORC diagrams (right) in the coordinates (h_c, h_u), measured at 0°, 10° and 20°. FORC diagrams at 30° and 40° were also added. Figures 3 and 4 show these results for sample S2 and S3, respectively.

As expected, the measurements carried out at 0° or at 180° correspond to standard FORC data, $M(H, H_R)$, with the FORCs delimited by the MHL (figure 2(left)). The colored reversal curves in the left panel are correlated with the colored 2D FORC diagram at the right. However, as the measurement angles depart from 0° or 180°, for example in the case of 20° (figure 2), the set of FORC curves starts to collapse making it difficult to distinguish one curve from another. This collapse begins as soon as the H_{eb} axis and the applied magnetic field direction are not aligned, and in particular at angles above ±20° with respect to 0° or 180°, the FORC data resembles a single curve. The FORC distribution is extremely noisy and its intensity averages to zero.

Thus, the AFORC results provide a direct proof about the homogeneity of the internal field axis distribution. In fact, to the best of our knowledge, this is the first time that AFORC has been used as an effective tool to indicate the quality of samples in regards to magnetic canting, frustrated magnetic domain misalignment, or variation of intrinsic interaction fields, in which a quantitative value of the spread in the out-of-axis internal fields is given here. This result can be compared with the AFORC results reported by Kashi *et al* [32, 33] on the angular variation and evolution of the IFD and CFD profiles of Co nanowire arrays. In that work, due to chemical inhomogeneity and finite size effects, reliable out-of-axis AFORC distributions were obtained up to 90°.

Comparing the AFORC results for the three samples, the following points were inferred. (i) This quantitative angular spread of the intrinsic interaction fields obtained by AFORC is the same for the three samples, with a cut-off at 20°. However, a qualitative interpretation can be extended up to 40°. (ii) The AFORC diagrams of the three samples reveal that the measurements in opposite directions (+180°) are symmetric, and those at ± angles are equal. Therefore, the discussion of the strength and nature of the multiple contributions of exchange bias field is confined to the angular range from 0 to 40°. (iii) The three samples show different AFORC feature distributions, and this is a fingerprint of each one related to their multilayer structure. A sharp FORC distribution is indicative of uniform strength and very narrow dispersion of internal fields along the applied magnetic field direction. Meanwhile, the broadening of the FORC distribution is indicative of multiple internal fields, with different field strengths, that are not aligned with the external field. For each sample, it is possible to observe different features of these distributions at 0° and
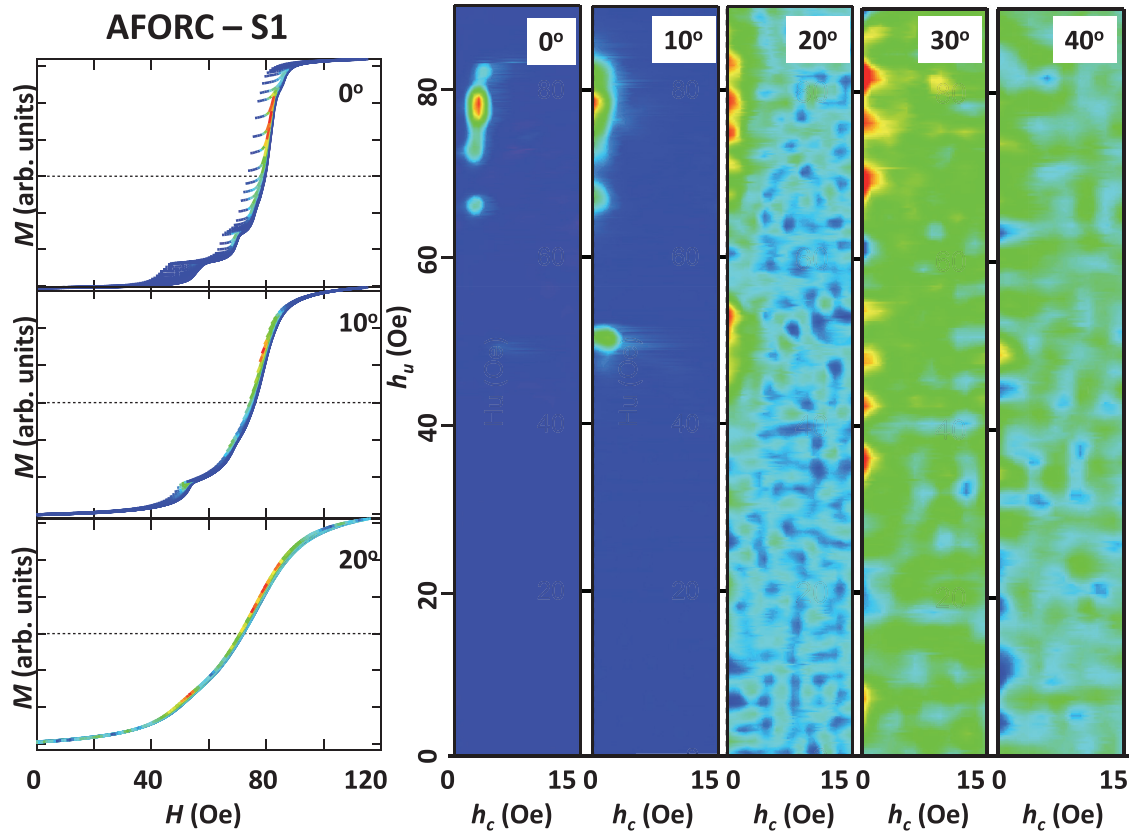
J. Phys. D: Appl. Phys. **50** (2017) 075002

R A Gallardo *et al*

Figure 2. Angular first order reversal curves (left) and their respective 2D FORC diagrams (right) in the coordinates (h_c, h_u) for sample S1, measured at 0°, 10°, and 20°. FORC diagrams at 30° and 40° were added.

up to 40°. This is due to the misalignment between the main internal field and the external field, which reinforces one component of the exchange bias field against other components. The analysis for each sample, with the internal field values and the full-width-at-half-maximum (σ_{FWHM}) value of the first mode, is given in the following paragraphs.

The AFORC diagrams of sample S1 show that, at 0° a main broad distribution is centered at an h_u-field of ~ 78 Oe ($\sigma_{\mathrm{FWHM}} = 4$ Oe), with a weak satellite distribution at ~ 67 Oe, and a very weak satellite at $h_u \sim 49$ Oe. At 10° these two last satellite distributions are reinforced, and the main h_u-field mode is broadened with $\sigma_{\mathrm{FWHM}} = 7$ Oe. Then, at 20° the main distribution at $h_u \sim 78$ Oe ($\sigma_{\mathrm{FWHM}} = 23$ Oe) is surrounded by other two distributions of the same strength, with a notable sharp increase of the distribution strength at $h_u \sim 49$ Oe. Also, as the angle increases, the center of the main distribution in the (h_c, h_u) diagram is shifted toward lower coercivity values. Progressively, at 30° and then at 40°, the diagrams show a multi-valley structure with several local minimum and maximum values, and this makes it difficult to obtain an accurate measurement of the main broad distribution.

The AFORC diagrams of sample S2 show that at 0° a main broad distribution with a vertical ridge is centered at $h_u \sim 39$ Oe ($\sigma_{\mathrm{FWHM}} = 2$ Oe), with a weak satellite distribution at ~ 28 Oe. At 10° the main distribution is more uniform in shape ($\sigma_{\mathrm{FWHM}} = 3$ Oe), without the vertical ridge, and it is shifted toward lower h_c values. At 20° this main distribution

is almost centered at $h_c = 0$ ($\sigma_{\mathrm{FWHM}} = 5$ Oe), and an additional peak is emerging at $h_u \sim 16$ Oe. At 30° and 40°, the diagrams show a multi-valley structure that is sharper than that of sample S1. At 30° the main distribution is considerably spread, and it shows a vertical ridge extending from 40 Oe to 46 Oe. Meanwhile, the secondary distribution is shifted up to 18 Oe. At 40° the multi-valley structure is accentuated, with several local maximum and minimum values, in which the main distribution ridge is extended from 40 Oe up to 50 Oe.

The AFORC diagrams of sample S3 show at 0° two superimposed distributions, between $h_u = 26$ Oe to 29 Oe, with a weak satellite distribution at ~ 18 Oe. This two peak overlap gives a σ_{FWHM} of 5 Oe. At 10° and 20° the main distribution is more uniform with a center position at h_u-field of 29 Oe ($\sigma_{\mathrm{FWHM}} = 4$ Oe). However, at 30° and 40° the main distribution is rapidly delocalized with a $\sigma_{\mathrm{FWHM}} \sim 9$ Oe, and with a vertical ridge from 15 Oe up to 40 Oe, respectively. In general, as the angle increases, the center of the main distribution in the (h_c, h_u)-diagram is shifted toward lower coercive field values.

From the AFORC diagrams of sample S1, S2, and S3, we extracted the H_{eb} values of each distribution visible on the FORC diagram. From a vertical cross-section of these 2D AFORC distributions we extracted the h_u profiles, which show splitting into two or three main magnetic distributions. The peaks seen in these distributions (labeled as h_u^{max} values) are related to the different exchange bias H_{eb} components
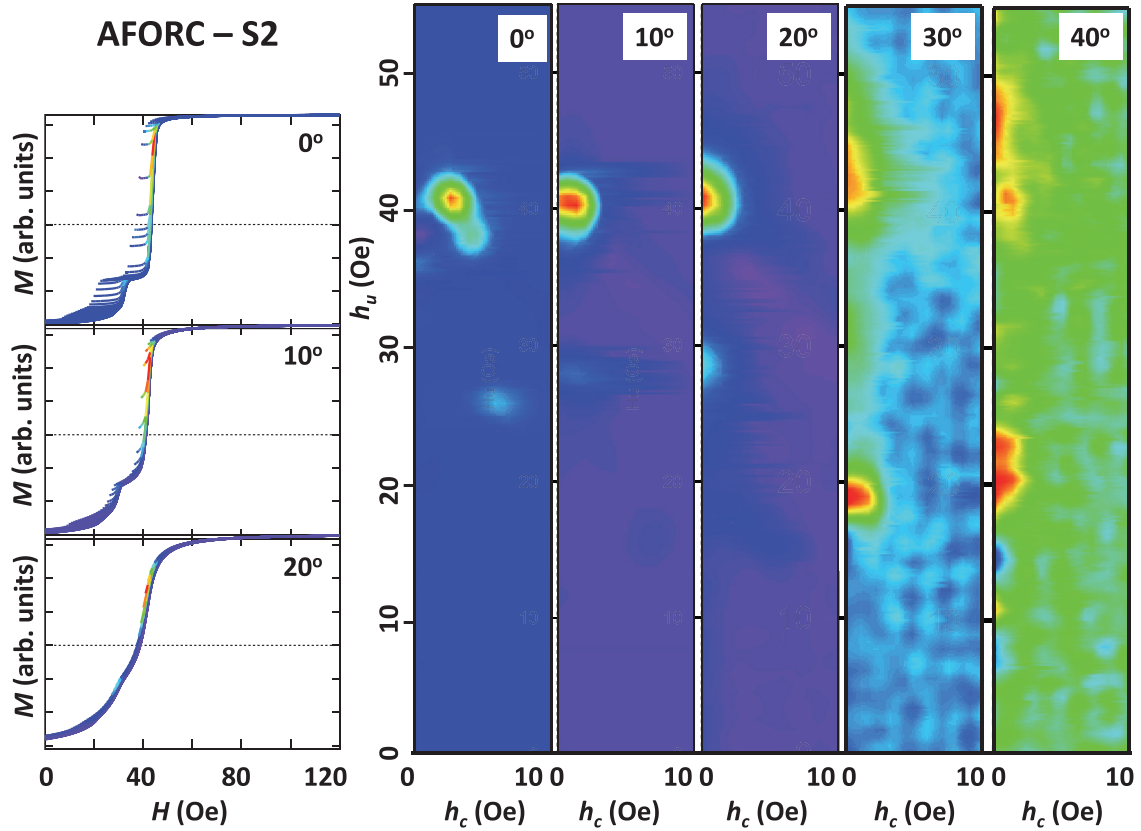
Figure 3. Angular first order reversal curves (left) and their respective 2D FORC diagrams (right) in the coordinates (h_c, h_u) for sample S2, measured at 0°, 10°, and 20°. FORC diagrams at 30° and 40° were added.
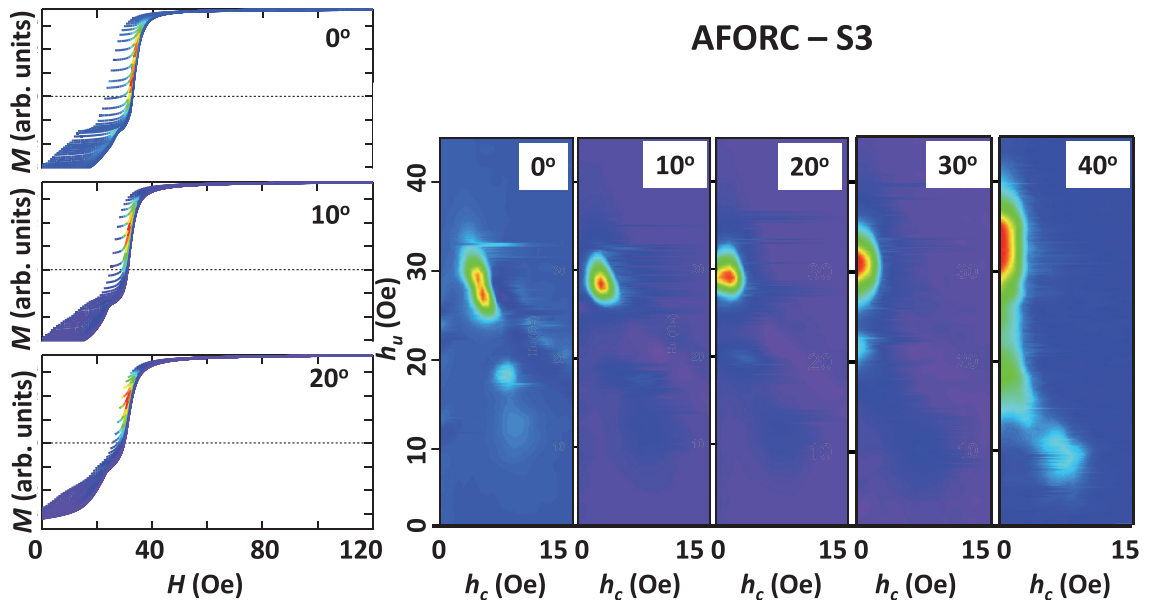

Figure 4. Angular first order reversal curves (left) and their respective 2D FORC diagrams (right) in the coordinates (h_c, h_u) for sample S3, measured at 0°, 10°, and 20°. FORC diagrams at 30° and 40° were added.

coexisting in each sample. The h_u profiles of sample S1, S2, and S3 are displayed in figure 5, obtained at 0°, 10°, and 20°. The vertical dotted lines in figure 5 correspond to the main h_u^{max} values. Due to the multi-valley structure that degrades

the FORC distributions, the h_u-profiles at 30° and 40° are not shown.

A comparison between these AFORC distributions and h_u-profiles show the complex interplay of internal fields, from
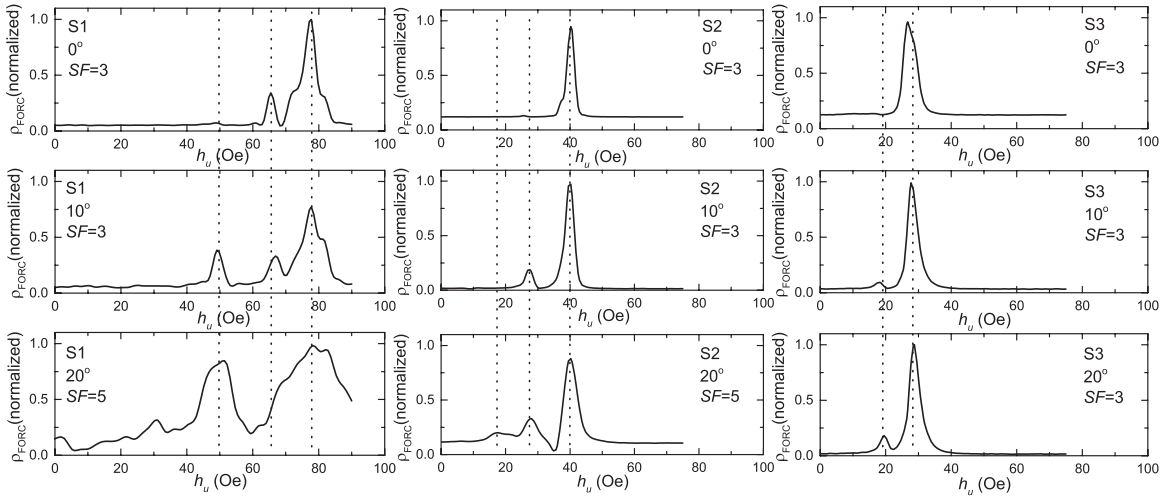
Figure 5. Vertical cross-section of the 2D FORC distributions of samples S1, S2 and S3, extracted at 0°, 10°, and 20°. SF is the optimized smoothing factor calculated by FORCinel.

Table 2. The H_{eb} values extracted from the AFORC distributions at 0°, 10° and 20°. The h_u^{max} means the center value of each distribution in the (h_c, h_u) 2D diagram.

	AFORC—H_{eb} values		
	h_u^{max} 1st mode (Oe)	h_u^{max} 2nd mode (Oe)	h_u^{max} 3rd mode (Oe)
S1	78	67	49
S2	39	28	16
S3	29	18	…

which the transition from multiple internal field components in S1 to a bimodal distribution in S3 is inferred. Even though the h_u-profile of sample S3 at 0° shows a single peak, this peak is a convolution of two or more contributions that are superimposed.

Table 2 summarizes the h_u^{max} peak field values, re-labeled as H_{eb}. These peak values obtained from the h_u-distributions at 0°, 10°, and 20°, are also in good qualitative agreement with the major hysteresis loops. For instance, sample S1 showed multiple steps in the MHLs, whereas sample S3 had smooth MHLs. The detailed analysis of these h_u^{max} peak field values and profile line-shape structure is beyond the scope of this article. A simulation tool or principal components analysis (FORCinel-PCA) is required for a proper interpretation of the internal fields of the multilayer samples.

FMR X-band angular variation

The in-plane angular variation of X-band FMR measurements are shown in figure 6, where at least two resonance lines can be seen. In the case of Samples S1 and S2, the most intense FMR line is observed near ∼ 1100 Oe, and a satellite line is present at higher fields and with a peak intensity of about 1/5 that of the principal resonance line. This satellite FMR line is clearly resolved in a narrow angular window centered at 0° and 180°. In contrast, the in-plane FMR angular variation of sample S3 shows a single line near 1100 Oe.

Figure 7 shows the in-plane angular variation of the resonant frequency H_{res} of the first and second modes, and table 3 summarizes the FMR parameters and values of H_{eb} for the first and second modes of sample S1 and S2, and the single mode of sample S3. A different H_{eb} and H_{RA} is observed for each mode. For all samples, the domain wall effective field used was $H_W = 1200$ Oe, which is strong enough to only produce a small deviation of the $\mathbf{M}_{AF}$ around the z-axis (less than 4°) during the in-plane rotation of the external field. The observed decrease of the resonant field near to 180° is predicted in the theoretical description and it is related to the uniaxial in-plane anisotropy H_K that reduces the FMR field when the magnetization is along the easy axis.

Overall, one can deduce that for sample S2, for instance, the second mode (squares and solid line) corresponds to the excitation of the bottom layer (the less coupled one), while the first mode (circles or dashed line) must be associated with the rest of the FM layers which have IrMn on both sides. Figure 8 gives a schematic representation of the magnetization behavior in the hysteresis loop. A similar behavior is detected for sample S1, where the FM bottom layer is the less coupled one. In sample S3, the two modes are very close together and therefore only one representative mode is detected (at $H_{eb} = 25$ Oe). Further, the value of rotatable field H_{RA} is lower in the 2nd modes than the 1st ones. This is reasonable according to the definition of the rotatable field, since the bottom layer (which is associated with the 2nd mode) is coupled to only one AFM layer and then a smaller rotatable anisotropy field is expected. Also, more than two modes can be detected, as shown in figure 9. These additional modes suggest a stepwise reversal of the films, in which the less coupled layer reverses first, then the adjacent one and so on. Thus, more than two modes are expected. Nonetheless, the fact that there are two modes with strong intensity indicates that the nucleation field for each of the upper layers is similar.

The angular dependence of exchange-bias field $H_{eb}(\varphi)$ (see equation (7)) is shown in figure 9 for samples S1, S2 and S3. It is clear that the FORC data show one additional mode compared to the FMR measurements. The magnetic parameters
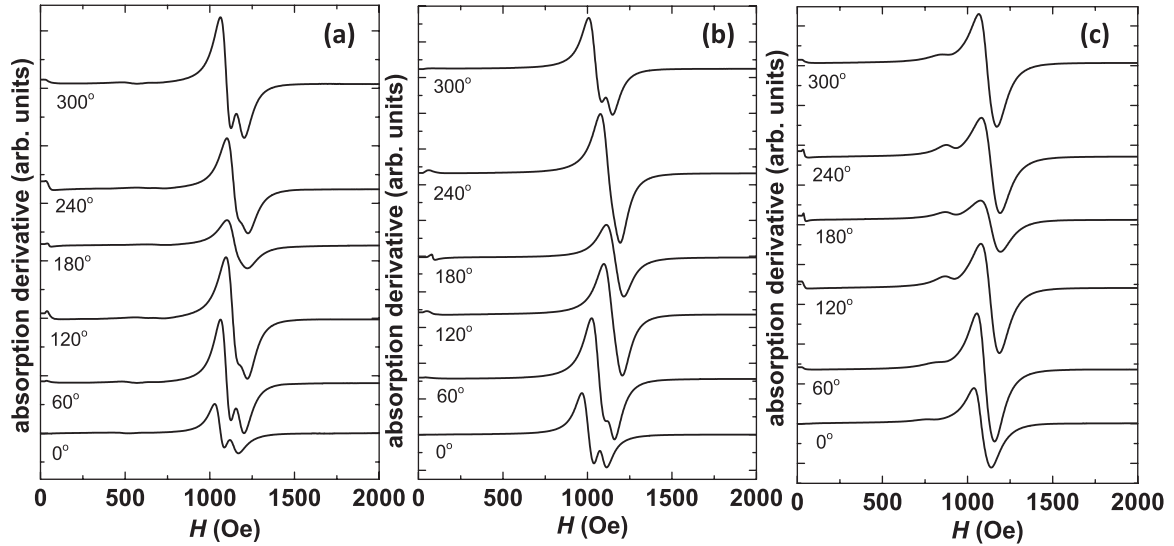
Figure 6. In-plane azimuthal angular variation of the X-band FMR spectra of samples (a) S1, (b) S2, and (c) S3. The angles are indicated on each curve. 0° and 180° means magnetic field parallel and antiparallel to the exchange-bias field, respectively.
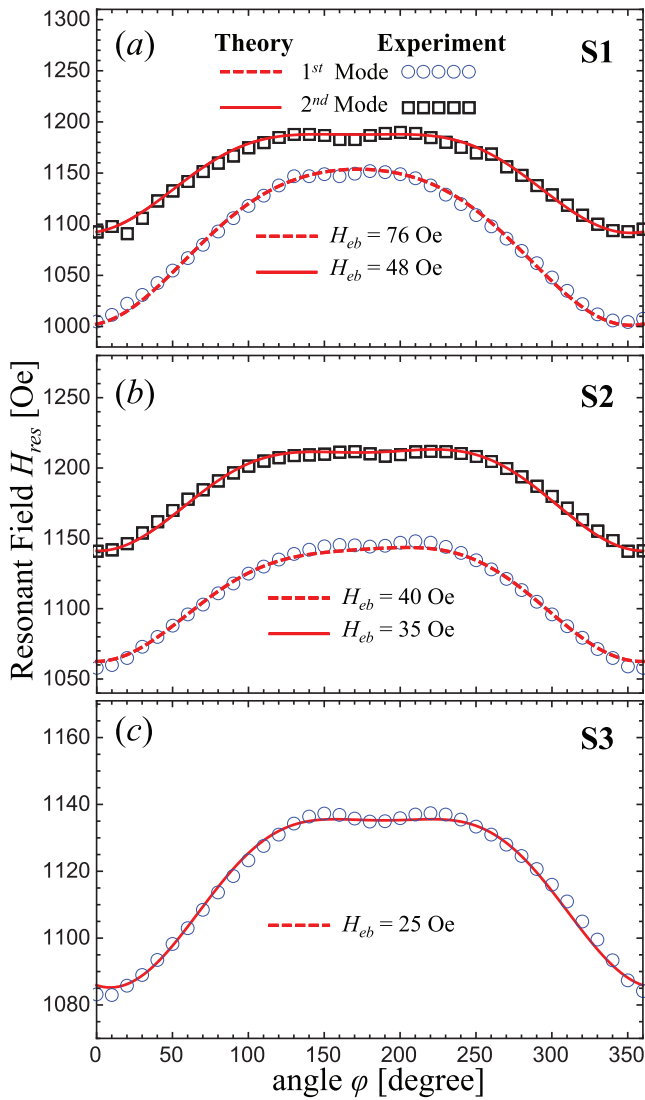

Figure 7. FMR first and second resonant field against φ for samples (a) S1, (b) S2 and (c) S3.

Table 3. Magnetic parameters determined from the fits to the FMR data.

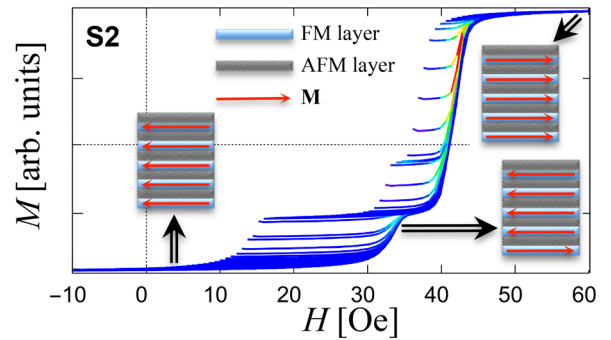| Sample	H_{eb} (Oe)	H_{RA} (Oe)	H_K (Oe)	φ_{AK} (°)	φ_K (°)	M_{eff} (emu cm^{-3})
S1						
1st mode	76	70	16	−8	−8	878
2nd mode	48	5	16	−8	−8	878
S2						
1st mode	40	79	13	2	−3	849
2nd mode	35	3	13	2	0	849
S3						
1st mode	25	44	8	9	9	875

Figure 8. Schematic representation of the magnetization in the multilayer system for sample S2. The steps in the loop are attributed to different degrees of coupling for each layer.

obtained from FORC and FMR data are shown in tables 2 (FORC) and 3 (FMR), respectively. There is good agreement in the exchange-bias field H_{eb} extracted from the first modes, but the other modes manifest some discrepancies. This difference can be explained due to the fact that, while in FMR technique the H_{eb} values are obtained from a direct measurement of the angular variation of the satellite resonance field,
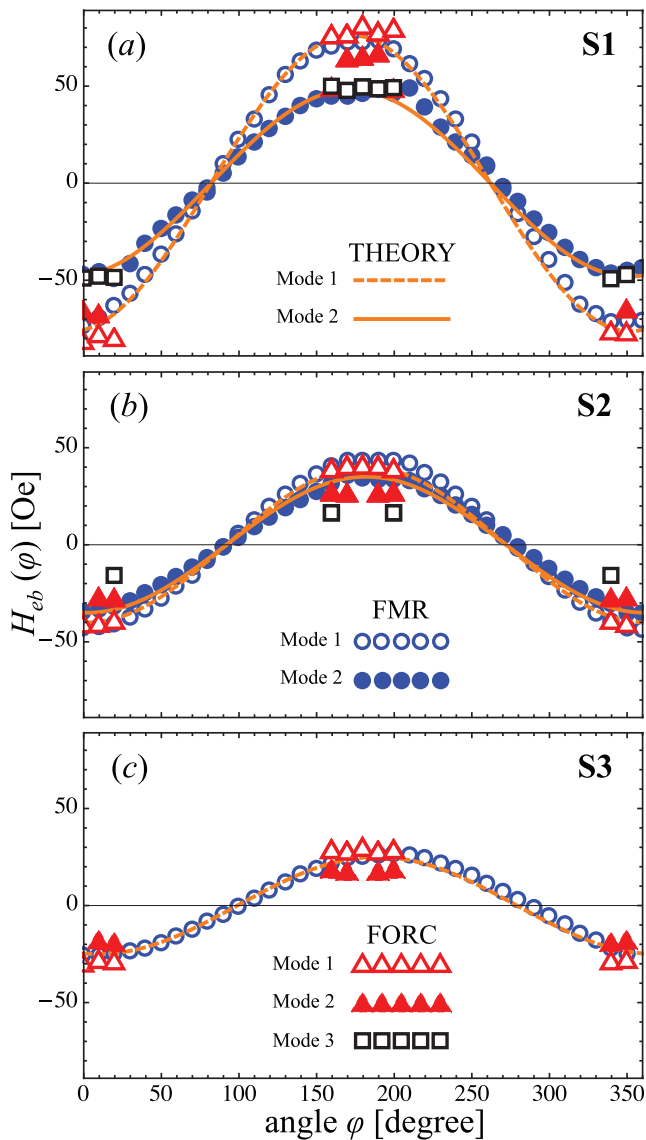
Figure 9. Angular dependence of the exchange-bias field of sample (a) S1, (b) S2 and (c) S3. In samples S1 and S2, FMR data show two modes, while three distinguishable modes are detected from FORC data. In sample S3, one mode is detected from FMR measurements, while two modes are obtained from FORC.

in the AFORC method these H_{eb} values are derived from the identification of the physical meaning of the mathematical hysterons. Thus, in sample S1 for example, the second and third modes extracted from FORC yield exchange-bias fields $H_{eb} = 67$ Oe and 49 Oe, respectively, while in the FMR data the second mode produces an EB field $H_{eb} = 48$ Oe. Hence, the second FMR mode appears to correspond to the third FORC mode.

Conclusions

The in-plane angular variation of (FeNi/IrMn)n multilayers has been studied by both static and dynamic measurement techniques, FORC and X-band FMR respectively.

The two X-band FMR modes corresponding to the bottom layer (coupled to IrMn on one side) and to the rest of the ferromagnetic layers (coupled on both sides) have been correlated with the distributions obtained via FORC characterization. The coexisting magnetic contributions in each multilayer sample were identified using the full FORC angular variation from 0° up to 360°. In spite of its limitations, the FORC angular variation proved to be a useful procedure, yielding two or three exchange-bias field values. These internal fields are related to different structural conditions and interfaces in the (FeNi/IrMn). Thus, the AFORC results provide a direct proof about the degree of homogeneity of the internal field axis distribution. In fact, to the best of our knowledge, this is the first time that AFORC has been used as an effective tool to indicate the quality of the samples in regards to magnetic canting, frustrated magnetic domain misalignment, or the distribution of intrinsic interaction fields, in which a quantitative value of the out-of-axis internal field spread is given here with a limit of 20°.

Overall, the main results are in good agreement with a modified theoretical model of domain-wall formation, where the angular variation and the degrees of coupling of the ferromagnetic layers have been well described and explained. The systematic study leads to a better understanding of the physics behind FM multilayer systems and allows detection of the influence of magnetic interactions produced by inhomogeneities existing at the antiferromagnet/ferromagnet interface during the in-plane angular variation.

References

[1] Meiklejohn W H and Bean C P 1957 *Phys. Rev.* **105** 904–13
[2] Nogués J and Schuller I K 1999 *J. Magn. Magn. Mater.* **192** 203–32
[3] Stamps R L 2000 *J. Phys. D: Appl. Phys.* **33** R247
[4] Kiwi M 2001 *J. Magn. Magn. Mater.* **234** 584–95
[5] Nogués J, Sort J, Langlais V, Skumryev V, Suriñach S, Muñoz J and Baró M 2005 *Phys. Rep.* **422** 65–117
[6] Parkin S, Jiang X, Kaiser C, Panchula A, Roche K and Samant M 2003 *Proc. IEEE* **91** 661–80
[7] Dubowik J, Stobiecki F, Gościańska I, Lee P Y, Paetzold A and Röll K 2005 *Eur. Phys. J.* B **45** 283–8
[8] Gloanec M, Rioual S, Lescop B, Zuberek R, Szymczak R, Aleshkevych P and Rouvellou B 2009 *Phys. Rev.* B **80** 220404
[9] da Silva R B, Viegas A D C, Nascimento V P, Corrêa M A, Schelp L F, Baggio-Saitovitch E and Sommer R L 2009 *Appl. Phys. Lett.* **94** 042501
[10] Radu F and Zabel H 2007 *Magnetic Heterostructures* (*Springer Tracts in Modern Physics* vol 227) ed H Zabel and S Bader (Berlin: Springer) pp 97–184

J. Phys. D: Appl. Phys. 50 (2017) 075002

R A Gallardo *et al*

[11] Mauri D, Siegmann H C, Bagus P S and Kay E 1987 *J. Appl. Phys.* **62** 3047–9

[12] Malozemoff A P 1987 *Phys. Rev. B* **35** 3679–82

[13] Nowak U, Usadel K D, Keller J, Miltényi P, Beschoten B and Güntherodt G 2002 *Phys. Rev. B* **66** 014430

[14] Mitsumata C, Sakuma A and Fukamichi K 2003 *Phys. Rev. B* **68** 014437

[15] Lederman D, Ramírez R and Kiwi M 2004 *Phys. Rev. B* **70** 184422

[16] Huang Z, Li S, Lin H, Zhang F and Du Y 2006 *J. Magn. Magn. Mater.* **303** e180–3 (*The 6th Int. Symp. on Physics of Magnetic Materials*)

[17] Rodríguez-Suárez R L, Vilela-Leão L H, Bueno T, Oliveira A B, de Almeida J R L, Landeros P, Rezende S M and Azevedo A 2011 *Phys. Rev. B* **83** 224418

[18] Rodríguez-Suárez R L, Vilela-Leão L H, Bueno T, Mendes J B S, Landeros P, Rezende S M and Azevedo A 2012 *Appl. Phys. Lett.* **100** 242406

[19] Stiles M D and McMichael R D 1999 *Phys. Rev. B* **59** 3722–33

[20] Phuoc N N, Hung L T, Xu F and Ong C K 2010 *J. Appl. Phys.* **108** 023909

[21] Béron F, Ménard D and Yelon A 2008 *J. Appl. Phys.* **103** 07D908

[22] Mayergoyz I 1986 *IEEE Trans. Magn.* **22** 603–8

[23] Mayergoyz I D 1986 *Phys. Rev. Lett.* **56** 1518–21

[24] Mayergoyz I D 2003 *Mathematical Models of Hysteresis and Their Applications* (*Electromagnetism*) ed I D Mayergoyz (New York: Elsevier)

[25] Pike C R, Roberts A P and Verosub K L 1999 *J. Appl. Phys.* **85** 6660–7

[26] Dobrotă C I and Stancu A 2013 *J. Appl. Phys.* **113** 043928

[27] Rotaru A, Lim J H, Lenormand D, Diaconu A, Wiley J B, Postolache P, Stancu A and Spinu L 2011 *Phys. Rev. B* **84** 134431

[28] Dumas R K, Li C P, Roshchin I V, Schuller I K and Liu K 2007 *Phys. Rev. B* **75** 134405

[29] Davies J E, Hellwig O, Fullerton E E, Denbeaux G, Kortright J B and Liu K 2004 *Phys. Rev. B* **70** 224434

[30] Khanal S, Diaconu A, Vargas J M, Lenormand D R, Garcia C, Ross C A and Spinu L 2014 *J. Phys. D: Appl. Phys.* **47** 255002

[31] Proenca M P, Ventura J, Sousa C T, Vazquez M and Araujo J P 2014 *J. Phys.: Condens. Matter* **26** 116004

[32] Jafari-Khamse E, Kashi M A and Ramazani A 2015 *Mater. Chem. Phys.* **159** 128–38

[33] Alikhani M, Ramazani A, Kashi M A, Samanifar S and Montazer A H 2016 *J. Magn. Magn. Mater.* **414** 158–67

[34] Geshev J, Nicolodi S, da Silva R B, Nogués J, Skumryev V and Baró M D 2009 *J. Appl. Phys.* **105** 053903

[35] García C, Florez J M, Vargas P and Ross C A 2011 *J. Appl. Phys.* **109** 07D735

[36] García C, Florez J M, Vargas P and Ross C A 2010 *Appl. Phys. Lett.* **96** 232501

[37] Smit J and Beljers H G 1955 *Phil. Res. Rep.* **10** 113

[38] Geshev J, Pereira L G and Schmidt J E 2001 *Phys. Rev. B* **64** 184411

[39] Harrison R J and Feinberg J M 2008 *Geochem. Geophys. Geosyst.* **9** 11